Journal of Materials Chemistry A

Cation-Disorder Zinc Blende Zn0.5Ge0.5P Compound and Zn0.5Ge0.5P-TiC-C composite as High-Performance Anode for Lithium-ion Batteries

Journal:	*Journal of Materials Chemistry A*
Manuscript ID	TA-ART-10-2020-010521.R1
Article Type:	Paper
Date Submitted by the Author:	03-Mar-2021

Complete List of Authors:	Liu, Guoping; Guangdong University of Technology, School of Materials and Energy; Zhaoqing University, College of Mechanical and Automotive Engineering Zhang, Lei; Georgia Institute of Technology, School of Materials Science and Engineering Zhou, Yucun; Georgia Institute of Technology, School of Materials Science and Engineering Soule, Luke; Georgia Institute of Technology, School of Materials Science and Engineering Mu, Yangchang; Guangdong University of Technology, School of Materials and Energy Li, Wenwu; Guangdong University of Technology, School of Materials and Energy Shi, Zhicong; Guangdong University of Technology, New Energy Materials and Devices

ARTICLE

Cation-Disorder Zinc Blende $Zn_{0.5}Ge_{0.5}P$ Compound and $Zn_{0.5}Ge_{0.5}P$-TiC-C composite as High-Performance Anode for Lithium-ion Batteries

Received 00th January 20xx,
Accepted 00th January 20xx

DOI: 10.1039/x0xx00000x

Guoping Liu,‡ [a, c] Lei Zhang,‡[b] Yucun Zhou,[b] Luke Soule, [b] Yangchang Mu,[a] Wenwu Li*[a] and Zhicong Shi*[a]

Designing a novel anode material with suitable elemental composition and bonding structure for improving the limited capacity and poor lithium-ion conductivity of lithium-ion batteries (LIBs) is still challenging. Here, guided by the first-principles calculations, we report a higher crystal symmetric, cation-disordered zinc blende $Zn_{0.5}Ge_{0.5}P$ anode material with high-capacity and high-rate capability owing to superior electron and lithium-ion transport compared to the parent allotrope chalcopyrite ZnGeP2. The $Zn_{0.5}Ge_{0.5}P$ anode exhibits a large specific capacity of 1435 mA h g^{-1} with a high initial Coulombic efficiency of 92%. An amorphization-conversion-alloying reaction mechanism is proposed based on *ex-situ* characterizations including X-ray diffraction (XRD), transmission electron microscopy (TEM), X-ray photoelectron spectroscopy (XPS), and Raman spectroscopy. During lithiation, the material phase-changes through Li_3P, LiZnGe, β-Li_2ZnGe, and α-Li_2ZnGe intermediates that provide suitable transport channels for fast diffusion of lithium ions. During delithiation, LiZn, $Li_{15}Ge_4$, and Li_3P nanoparticles reassemble into $Zn_{0.5}Ge_{0.5}P$. A $Zn_{0.5}Ge_{0.5}P$-TiC-C composite with finer particle size and enhanced electronic conductivity exhibits an initial specific capacity of 1076 mA h g^{-1} and a capacity retention of 92.6% after 500 cycles.

Introduction

Recent increases in technology electrification require the development of lithium-ion batteries (LIBs) with higher specific energy densities than are currently available.[1, 2] Intercalation reaction-type anode materials, e.g. LiC_6[3, 4] and $Li_4Ti_5O_{12}$,[5, 6] do not have sufficient Li-ion storage capacities to meet these requirements.[7] Research efforts have been devoted to using alloying reaction-type anodes due to their higher capacities.[8, 9] Single elemental anodes, such as Si, experience large volume changes and poor lithium-ion transport that limits their rate-capability.[10] Multi-element anodes have reduced volume changes during lithiation and have more suitable lithium-ion transport than single-element anodes, giving them high energy densities, high power capabilities, and high stability on repeated cycling.[11, 12]

Lithium alloying materials such as Zn,[13, 14] Ge,[15, 16] and P[17, 18] have been investigated as potential candidates due to their high theoretical capacity (LiZn: 409 mA h g^{-1}, $Li_{3.75}Ge$: 1381 mA h g^{-1},Li_3P: 2591mA h g^{-1}). Zn has a lithium reaction potential of 0.2 V (*vs.* Li^+/Li). The reaction proceeds through four intermediate phases giving rise to four voltage plateaus that hinder lithium diffusion.[13] Ge has a higher storage capacity than Zn as it can react with 3.75 Li. However, pure Ge anodes experience a volume change of up to 343% that results in particle cracking.[19] P exhibits a reaction potential of 0.7 V (vs. Li^+/Li) due to its high electronegativity. Additionally, it has been found that the Li_3P facilities lithium diffusion.[20]

To fully benefit from the properties of each element, they can be combined in binary or tertiary compounds. Binary compounds, such as ZnP_2,[21, 22] Zn_3P_2,[23, 24] GeP,[25, 26] GeP_3,[27, 28] and GeP_5,[29, 30] have been widely studied for lithium storage. When these binary compounds react with lithium, P first reacts to form Li_xP then Li reacts with Zn/Ge to form metal alloys such as LiZn and $Li_{15}Ge_4$. For ternary compounds, cation ordering can be used to modulate the intrinsic properties and electrochemical characteristics of the anodes during lithiation.[31, 32]

The Zn-Ge-P compounds are a member of the ternary $A^{II}B^{IV}C^{V}_2$ materials family and have two allotropes: chalcopyrite $ZnGeP_2$ and zinc blende $Zn_{0.5}Ge_{0.5}P$.[33-35] Through suitable processing, ordered chalcopyrite $ZnGeP_2$ (I-42d) and disordered zinc blende $Zn_{0.5}Ge_{0.5}P$ (F-43m) can be synthesized.[35]

In this work, first-principles calculations were used to compare the electron and lithium-ion transport capabilities of $ZnGeP_2$ and $Zn_{0.5}Ge_{0.5}P$. Zinc blende $Zn_{0.5}Ge_{0.5}P$ has metallic conductivity with no band gap while chalcopyrite $ZnGeP_2$ is a semiconductor with a band gap of 0.93 eV. Zinc blende $Zn_{0.5}Ge_{0.5}P$ exhibits a lower average lithium-ion diffusion energy barrier (~ 0.20 eV) than chalcopyrite $ZnGeP_2$ (~ 0.45 eV). In light of these findings, zinc-blende $Zn_{0.5}Ge_{0.5}P$ was synthesized using

[a] School of Materials and Energy, Guangdong University of Technology, Guangzhou 510006, PR China. E-mail: 962793489@qq.com (W. Li), zhicong@gdut.edu.cn (Z. Shi)
[b] School of Materials Science and Engineering, Georgia Institute of Technology, Atlanta, GA 30332, USA.
[c] College of Mechanical and Automotive Engineering, Zhaoqing University, PR China

† Electronic Supplementary Information (ESI) available: First principles calculation details; calculation details of D_{Li}; SEM, TEM, and SAED images of $Zn_{0.5}Ge_{0.5}P$, and long cycling performance of $Zn_{0.5}Ge_{0.5}P$ anode. See DOI: 10.1039/x0xx00000x

‡ G. Liu and L. Zhang contributed equally to this work.

high-energy ball milling and investigated as an anode material for LIBs. Reaction mechanisms were investigated using electrochemical techniques such galvanostatic charging and discharging and the galvanostatic intermittent titration technique (GITT), and phase structure analysis using X-ray diffraction (XRD), high-resolution transmission electron microscope (HR-TEM), X-ray photoelectron spectroscopy (XPS), and Raman spectroscopy. It was found that zinc-blende $Zn_{0.5}Ge_{0.5}P$ experiences an amorphization-conversion-alloying reaction mechanism with Li_3P, LiZnGe, β-Li_2ZnGe, and α-Li_2ZnGe reaction intermediates. TiC and C were used with $Zn_{0.5}Ge_{0.5}P$ to fabricate a $Zn_{0.5}Ge_{0.5}P$-TiC-C nanocomposite with enhanced electrochemical performance.[14, 36, 37]

Experimental

Materials synthesis

$Zn_{0.5}Ge_{0.5}P$ was synthesized using mechanochemical methods. Stoichiometric amounts of Zn (600 mesh, 99.99% metals basis, Aladdin), Ge (≥ 200mesh, 99.999% metals basis, Aladdin), red P (100 mesh, 99% metals basis, Alfa Aesar), and stainless steel balls with a diameter of 10 mm were added to a stainless steel grinding bowl (capacity of 500 mL) with a powder-to-ball weight ratio of 1:25. The bowl was filled in an Ar filled glovebox. High-energy ball milling was conducted using a Planetary-Mono-Mill (Fritsch P6) at the speed of 450 rpm. The milling time was 30 min with 25 min rest between each cycle, giving a total milling time of 0.5 h, 1 h, and 8 h depending on desired synthesis. $Zn_{0.5}Ge_{0.5}P$-C, $Zn_{0.5}Ge_{0.5}P$-TiC, and $Zn_{0.5}Ge_{0.5}P$-TiC-C composites were prepared by a similar ball-milling condition with a milling time of 3 h in a mass ratio of 70:30 ($Zn_{0.5}Ge_{0.5}P$:C, $Zn_{0.5}Ge_{0.5}P$:TiC) or 70:15:15 ($Zn_{0.5}Ge_{0.5}P$:TiC:C). Carbon used for the composites was synthesized by ball milling commercial graphite (≥ 100mesh, 99.95% metals basis, Aladdin) for 20 h under the same condition as that of $Zn_{0.5}Ge_{0.5}P$.

Materials characterization

Phase characterization was performed using X-ray diffraction (XRD) on a Bruker-D8 Advance powder diffractometer equipped with Cu $K\alpha$ radiation ($\lambda = 1.541$ Å). The morphology and structure of the materials were observed using a field-emission scanning electron microscopy (SEM) Hitachi-SU8220 microscope and transmission electron microscopy (TEM) on a FEI Talos F200S microscope with selected area electron diffraction (SAED). Raman spectra were collected on a micro-confocal Jobin Yvon LabRAM HR Evolution Raman spectrometer with a 532 nm excitation laser. The chemical composition and the bonding structure were determined using X-ray photoelectron spectroscopy (XPS) on a Thermo Fisher Escalab 250Xi.

Electrochemical measurements

$Zn_{0.5}Ge_{0.5}P$ electrode films were prepared by mixing $Zn_{0.5}Ge_{0.5}P$, acetylene black, and Li-PAA binder in a weight ratio of 70:20:10 followed by casting onto a Cu foil. The composite $Zn_{0.5}Ge_{0.5}P$-C, $Zn_{0.5}Ge_{0.5}P$-TiC, and $Zn_{0.5}Ge_{0.5}P$-TiC-C electrode films were prepared by mixing the composite with Li-PAA in a weight ratio of 90:10 followed by casting on Cu foils. Electrode films were dried under vacuum at 100 °C for 10 h. The electrodes mass loading was 1.5 – 2 mg cm^{-2}. Electrochemical properties of the electrodes were tested using coin cells (CR2032) with lithium metals as both counter and reference electrodes and using 1 M $LiPF_6$ in EC-DEC (1:1 mixed volume) as the electrolyte. Galvanostatic discharge/charge tests of the coin cells were conducted using LAND battery tester (Wuhan LAND Electronics Co. Ltd., China). The galvanostatic intermittent titration technique (GITT) test of the $Zn_{0.5}Ge_{0.5}P$ electrode was conducted at a pulse of 50 mA g^{-1} for 0.5 min with a 4 h relaxation period between each pulse on a LAND battery tester. Electrochemical impedance spectroscopy (EIS) was measured in the frequency range of 10 mHz - 100 KHz with an AC potential amplitude of 5 mV using a Solartron electrochemical workstation.

First principles calculation

First principles calculations of $Zn_{0.5}Ge_{0.5}P$ and $ZnGeP_2$ were conducted in the Vienna ab initio simulation package.[38] The calculation details can be found in The Electronic Supplementary Information (ESI).

Results and discussion

There are two ternary Zn, Ge, and P compound allotropes, $ZnGeP_2$ and $Zn_{0.5}Ge_{0.5}P$. $Zn_{0.5}Ge_{0.5}P$ has a zinc blende cubic structure with Zn and Ge ions randomly distributed on the cation position. $ZnGeP_2$ has an ordered tetragonal chalcopyrite structure in which the Zn and Ge ions occupy different metal sub-lattice. The cubic zinc-blende structure $Zn_{0.5}Ge_{0.5}P$ is more challenging to synthesize than $ZnGeP_2$ because it is typically only stable under high-pressure or high-temperature.[39] To get insights into the influence of structural transformation on their properties, first-principles calculations based on density functional theory (DFT) were used to study the electronic structure, elastic properties, and Li-ion diffusion mechanism of $Zn_{0.5}Ge_{0.5}P$ and $ZnGeP_2$. Firstly, as shown in **Fig. 1a**, the total electronic density of state (DOS) results suggest that there is no band gap for $Zn_{0.5}Ge_{0.5}P$, showing metallic conductivity, while $ZnGeP_2$ is a semiconductor with a band gap of 0.93 eV. As a result, the $Zn_{0.5}Ge_{0.5}P$ exhibits a much better electronic transport capability than that of $ZnGeP_2$. Secondly, regarding elastic properties, as seen in **Fig. 1b**, $Zn_{0.5}Ge_{0.5}P$ has smaller elastic moduli values than $ZnGeP_2$ in all directions, which indicates a softer bond binding of $Zn_{0.5}Ge_{0.5}P$, and this is beneficial to lithium-ion transport. Thirdly, the Li-ion transport paths and corresponding energy barriers of $Zn_{0.5}Ge_{0.5}P$ and $ZnGeP_2$ were calculated, as shown in **Fig. 1c** and **1d**. It is seen that the Li-ion diffusion energy barriers of $Zn_{0.5}Ge_{0.5}P$ are only 0.26 eV and 0.13 eV. The same barriers have a value of 0.3 eV and 0.61 eV in $ZnGeP_2$. To recap, both electron and lithium-ion transport capability in $Zn_{0.5}Ge_{0.5}P$ are better than those in chalcopyrite structured $ZnGeP_2$. Also, $Zn_{0.5}Ge_{0.5}P$ has a higher symmetry than $ZnGeP_2$ (F-43m compared to I-42d), which

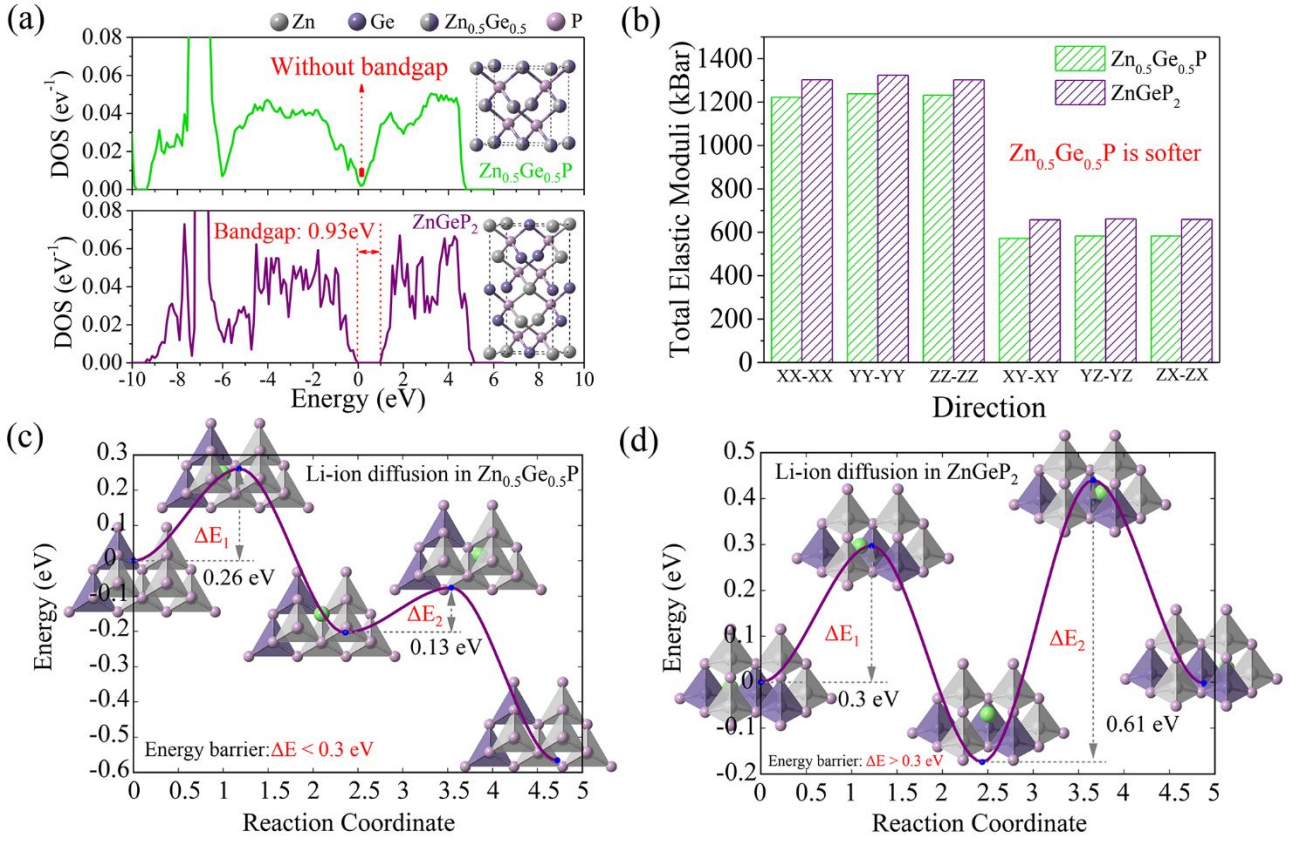

Fig. 1 (a) DFT calculation results on the electronic density of state (DOS) of zinc blende $Zn_{0.5}Ge_{0.5}P$ and chalcopyrite $ZnGeP_2$. (b) DFT calculation results of the total elastic moduli of $Zn_{0.5}Ge_{0.5}P$ and $ZnGeP_2$. Lithium-ion diffusion path and corresponding energy barrier of $Zn_{0.5}Ge_{0.5}P$ (c) and $ZnGeP_2$ (d).

indicates a more homogenous volume change upon reaction with lithium.

Based on the theoretical calculation results, $Zn_{0.5}Ge_{0.5}P$ was selected and tested as an anode material in LIBs. As shown in **Fig. 2a**, $Zn_{0.5}Ge_{0.5}P$ was synthesized mechanochemically by combining hexagonal-structured Zn, cubic-structured Ge, and amorphous red P. Under high-energy ball-mill conditions, pressures of up to 6 GPa and temperatures up to 200 °C can be generated.[40] As shown in **Fig. 2b**, in the first 20 minutes of milling, $Zn_{0.5}Ge_{0.5}P$ was formed with the phase purity increasing with increasing ball-milling time. Crystalline $Zn_{0.5}Ge_{0.5}P$ was investigated using XRD and Rietveld refinement, as shown in **Fig. 2c**. Diffraction peaks can be well indexed to zinc blende structured $Zn_{0.5}Ge_{0.5}P$ phase with the space group of F-43m (PDF #04-001-5192) and lattice parameters of $a = b = c = 5.442$ Å and $\alpha = \beta = \gamma = 90°$. Selected-area electron diffraction (SAED) pattern of the synthesized $Zn_{0.5}Ge_{0.5}P$ is shown in **Fig. S1.** A series of concentric circles are consistent with the above XRD result. The average grain size of the synthesized $Zn_{0.5}Ge_{0.5}P$ is ~ 13.5 nm as calculated by the Scherrer formula according to the low diffraction angle plane of (111), This is consistent with the HR-TEM analysis result shown in **Fig. S2**. As observed in TEM (**Fig. S3**) and SEM (**Fig. S4**) images, the primary $Zn_{0.5}Ge_{0.5}P$ nano particles tend to aggregate into micro-sized particles with a size ranging from 200 nm to 20 μm.

To exploring the electrochemical performances of $Zn_{0.5}Ge_{0.5}P$, galvanostatic charge and discharge tests were performed in half-cells *vs.* Li foil. As shown in **Fig. 2d**, the first discharge shows a specific capacity of 1,435 mA h g^{-1} with an average working potential of 0.46 V, which is lower than that of pure P (0.7V *vs.* Li/Li^+). The discharge curve of $Zn_{0.5}Ge_{0.5}P$ is smoother than of a pure Zn anode, indicating a more moderate phase transformation process between the potential-dependent intermediates during the lithiation process. During the first charge process, $Zn_{0.5}Ge_{0.5}P$ exhibits a reversible capacity of 1,309 mA h g^{-1} giving an initial Coulombic efficiency (ICE) of 92%. The first discharge specific capacity of the $Zn_{0.5}Ge_{0.5}P$ is close to the theoretical capacity of 1,438 mA h g^{-1} calculated based on the formation of LiZn, $Li_{15}Ge_4$, and Li_3P phases, which suggests a high utilization. **Fig. 2e** and **2f** show the cycling performance and EIS plots of $Zn_{0.5}Ge_{0.5}P$ compared with mixed Zn-Ge-P powder and ball-milled intermediate products of Zn-Ge-P@3h, Zn-Ge-P@1h. $Zn_{0.5}Ge_{0.5}P$ shows the best cycling performance and the lowest charge transfer resistance among the compositions. **Fig. S5** shows the extended cycling performance of $Zn_{0.5}Ge_{0.5}P$, where a 50% (718 mA h g-1) capacity retention is found after 30 cycles with a capacity retention of 20% (278 mA h g^{-1}) after 200 cycles. Such rapid capacity fade can be attributed to the massive volume change and side reactions between the anode material and electrolyte.

To getting a deeper understanding of the lithiation and delithiation mechanism, electrochemical techniques and phase structure analysis were performed on $Zn_{0.5}Ge_{0.5}P$ to study the material's reaction with Li. According to the dQ/dV plot shown in **Fig. 2g**, the lithiation reactions occur in three potential ranges, (I): a small peak region at 2 - 0.6 V, (II): a broad, strong

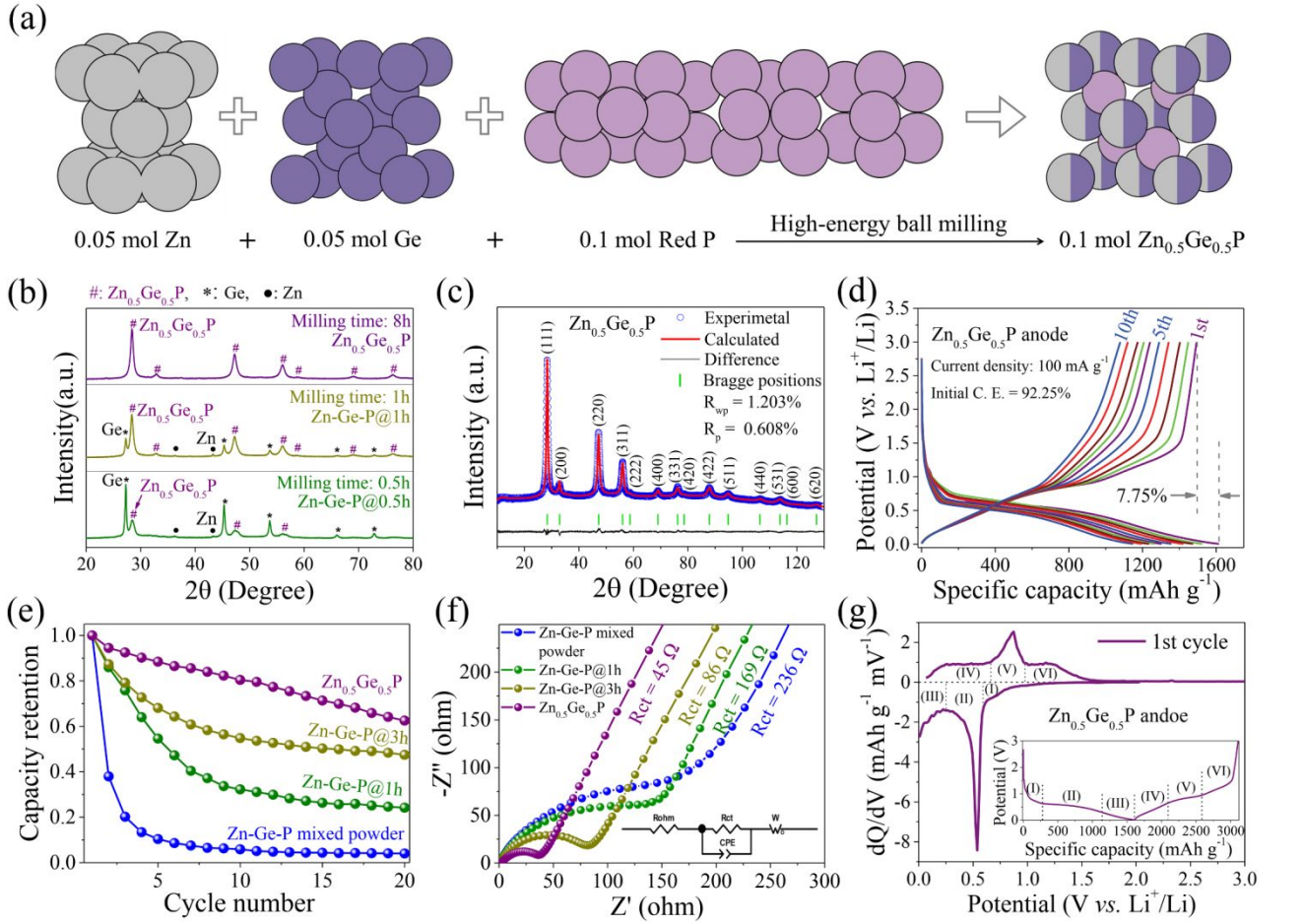

Fig. 2 (a) Schematic diagram of zinc blende $Zn_{0.5}Ge_{0.5}P$ combining from hexagonal Zn, cubic Ge, and amorphous red P by high-energy ball milling; (b) XRD patterns evolution of $Zn_{0.5}Ge_{0.5}P$ during the synthesis process; (c) XRD Rietveld refinement of the as-synthesized zinc blende $Zn_{0.5}Ge_{0.5}P$ phase; (d) Galvanostatic discharge-charge profiles of $Zn_{0.5}Ge_{0.5}P$ *vs.* Li using 1 M $LiPF_6$ in EC-DEC as the electrolyte; (e) The cycling performance comparison of the zinc blende $Zn_{0.5}Ge_{0.5}P$, Zn-Ge-P@3h, Zn-Ge-P@1h, and the Zn-Ge-P mixed powder anodes; (f) The EIS comparison of the zinc blende $Zn_{0.5}Ge_{0.5}P$, Zn-Ge-P@3h, Zn-Ge-P@1h, and the Zn-Ge-P mixed powder anodes; (g) First lithiation and delithiation dQ/dV plot of zinc blende $Zn_{0.5}Ge_{0.5}P$ *vs.* Li with corresponding voltage profile insert.

peak at 0.6 - 0.25 V, and (III): a small peak at 0.25 - 0 V. During delithiation, three potential ranges are also observed, (IV): a stable current region of 0 - 0.65 V, (V): a strong oxidation peak region of 0.65 - 1 V, and (VI): a final delithiation region of 1-2 V. These regions are marked accordingly on the first charge-discharge curve shown in the inset of **Fig. 2g**.

To further investigate the reactions and intermediates in these regions, ex-situ XRD, Raman, TEM, and XPS were conducted. According to the ex-situ XRD results shown in **Fig. 3a** and **3b**, the pristine electrode shows the main diffraction peaks of the zinc blend structure located at 28.4°, 32.9°, 47.2°, and 56.0° under open circuit voltage (OCV). When discharged to 0.6 V, the intensity of these peaks decrease and disappear at 0.53 V, indicating that the crystalline $Zn_{0.5}Ge_{0.5}P$ amorphizes when forming $Li_xZn_{0.5}Ge_{0.5}P$ ($0 \leq x \leq 1$, calculated from the corresponding specific capacity). After being discharged to 0.4 - 0.3 V, new diffraction peaks generated are indexed to Li_3P, LiZnGe, β-Li_2ZnGe and α-Li_2ZnGe. When fully discharged to 0 V, LiZnGe, α-Li_2ZnGe, β-Li_2ZnGe diffraction peaks disappear and LiZn and $Li_{15}Ge_4$ phases formed, suggesting that LiZnGe, α-Li_2ZnGe, and β-Li_2ZnGe intermediates further react with Li. It should be noted that the diffraction peaks of Li_3P are obvious, but the peaks of LiZnGe, α-Li_2ZnGe, β-Li_2ZnGe, LiZn and $Li_{15}Ge_4$ were shown with broad peaks. This is because there are many kinds of lithiated phases at 0.4 V or 0 V, and their standard diffraction peaks, as shown in Fig. S6, are very closed or overlapped. During charging, the LiZn and $Li_{15}Ge_4$ phases gradually disappear and LiZnGe, α-Li_2ZnGe, and β-Li_2ZnGe intermediates reform when charged to 0.7 V. After charging to 1.1 V, the electrode becomes amorphous again. Finally, crystalline $Zn_{0.5}Ge_{0.5}P$ is reformed when fully charged back to 3 V. Ex-situ XRD results indicate that $Zn_{0.5}Ge_{0.5}P$ exhibits a high specific capacity due to the formation of the LiZn, $Li_{15}Ge_4$, and Li_3P reaction intermediates.

The lithium-ion diffusion coefficient (D_{Li}) is an important parameter to qualify reaction kinetics.[41, 42] The potential-dependent D_{Li} was investigated and obtained using the GITT test. The calculation details of D_{Li} is mentioned in the Electronic Supplementary Information (ESI). The results are shown in **Fig. 3c**. At the beginning of the discharging process, the D_{Li} decreases with the increasing x value of $Lixn_{0.5}Ge_{0.5}P$, which can be attributed to the increasing lithium concentration within the $Zn_{0.5}Ge_{0.5}P$ electrode. The reduced lithium concentration difference makes further Li-ion intercalation and diffusion more

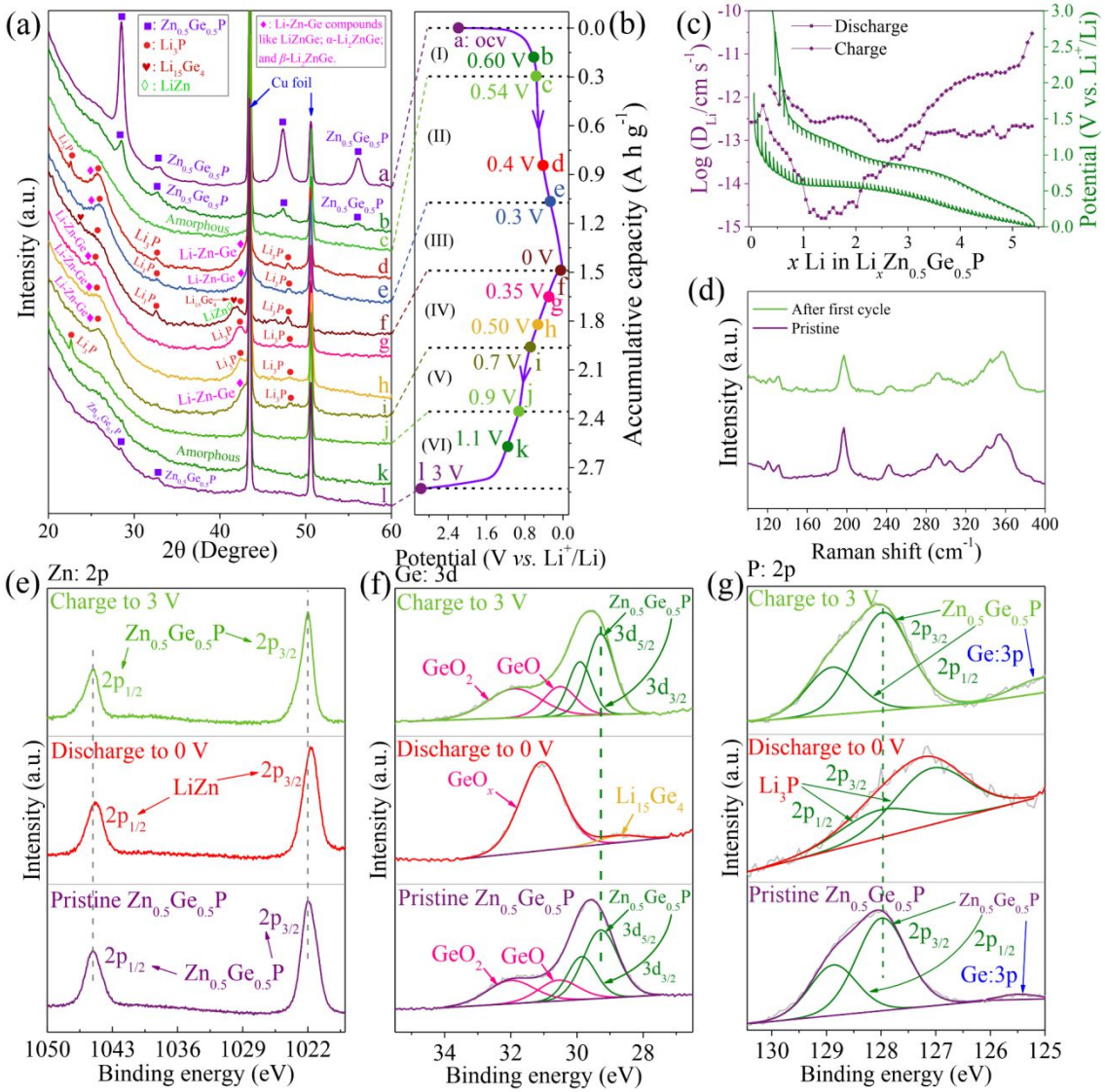

Fig. 3 (a) and (b) *Ex-situ* XRD results of the $Zn_{0.5}Ge_{0.5}P$ electrode during the first cycle with the voltage curve and corresponding potential regions and points; (c) Log of the lithium diffusion coefficient in $Zn_{0.5}Ge_{0.5}P$ anode determined *via* GITT test with respect to lithium content during first discharging-charging cycle and the voltage curve obtained from GITT test; (d) *Ex-situ* Raman spectroscopy of the $Zn_{0.5}Ge_{0.5}P$ electrode during the first discharging-charging cycle; (e), (f), and (g) *Ex-situ* XPS results of Zn 2p, Ge 3d, and P 2p of $Zn_{0.5}Ge_{0.5}P$ electrode during the first discharging-charging cycle.

difficult until all $Zn_{0.5}Ge_{0.5}P$ is transformed to the amorphous state with an x value equal to 1. Within $1 \leq x \leq 2$, LiZnGe and Li_3P intermediates are formed, resulting in bond breaking of Zn-P and Ge-P with P then reacting with Li to form Li_3P and Zn and Ge reacting to form LiZnGe. This process is kinetically limited,[43] and thus within the $1 \leq x \leq 2$, the D_{Li} drops. When $x \geq 2$, the new phases of Li_3P, LiZnGe, α-Li_2ZnGe, β-Li_2ZnGe gradually generated, and all these electrochemical intermediates are lithium-ion conductors,[42, 44] thus accelerating the Li-ion diffusion. When $x \geq 3.4$, D_{Li} keeps steady at a high level until discharged to 0 V. During the charging process, the D_{Li} gradually decreased until $x \leq 2.4$, which can be attribute to the reduced amount of the Lithium-ion conductors of the Li_3P, LiZnGe, α-Li_2ZnGe, and β-Li_2ZnGe. Additionally, two semi-circular evolutions of D_{Li} versus x is observed at the $1 \leq x \leq 2.3$ and $3 \leq x \leq 5$. This phenomenon is commonly observed in layered structure solids and can be explained in terms of ion-ion repulsion in the interlayer space. Therefore, the semicircle at $3 \leq x \leq 5$ is related to the Li_3P, and the semicircle at $1 \leq x \leq 2.3$ is associated with the LiZnGe and β-Li_2ZnGe.[42]

The ex-situ Raman and XPS results further demonstrate the structural reversibility of the reaction of $Zn_{0.5}Ge_{0.5}P$ with Li. As shown in **Fig. 3d**, the Raman peaks of the pristine $Zn_{0.5}Ge_{0.5}P$ are located at 122, 130, 197, 243, 292, 344, and 356 cm^{-1}.[45] These peaks reappear after first cycling, validating the high reversibility of the $Zn_{0.5}Ge_{0.5}P$ anode. The ex-situ XPS results show the structural reversibility of $Zn_{0.5}Ge_{0.5}P$. As shown in **Fig. 3e-g**, Zn (2p), Ge (3d), and P (2p) binding states of the pristine $Zn_{0.5}Ge_{0.5}P$ are consistent with the previous reports.[46] When discharged 0 V, the binding energy of the Zn (2p), Ge (3d), and P (2p) become consistent with the lithiation products of LiZn, $Li_{15}Ge_4$, and Li_3P respectively. Due to the high reactivity of the $Li_{15}Ge_4$ species with air, some germanium oxide is also detected. When charged to 3 V, the binding energy of the Zn (2p), Ge (3d),

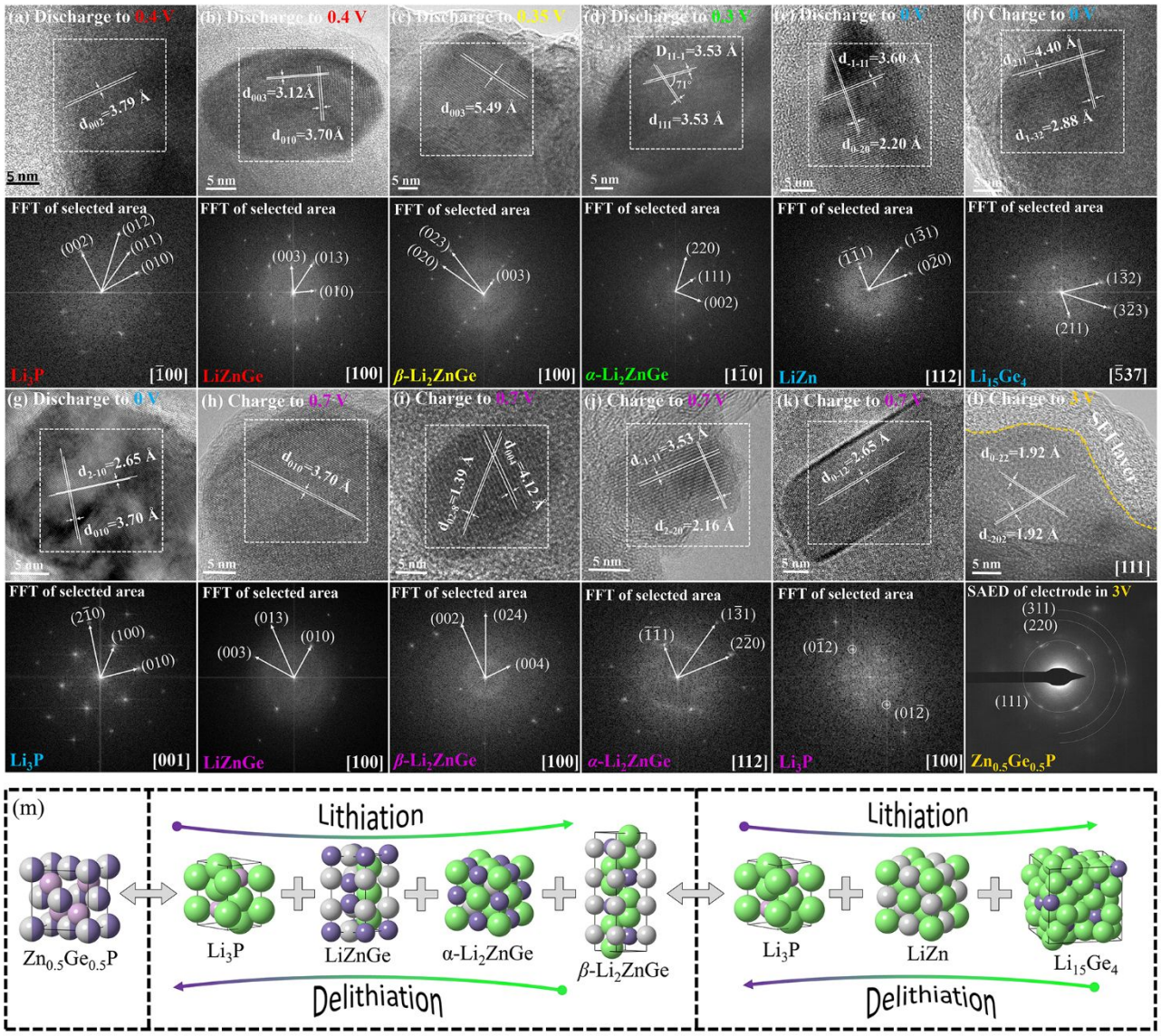

Fig. 4 *Ex-situ* HR-TEM images and corresponding FFT patterns of $Zn_{0.5}Ge_{0.5}P$ electrode collected at various discharge-charge states during the first cycle. Discharging: (a) Li_3P, (b) LiZnGe, (c) β-Li_2ZnGe, (d) α-Li_2ZnGe, (e) LiZn, (f) $Li_{15}Ge_4$, (g) Li_3P; Charging: (h) LiZnGe, (i) β-Li_2ZnGe, (j) α-Li_2ZnGe, (k) Li_3P, and (l) $Zn_{0.5}Ge_{0.5}P$ with SAED patterns. (m) Schematic illustration of electrochemical reaction mechanism between $Zn_{0.5}Ge_{0.5}P$ and Li.

and P (2p) shift back to the original position that is consistent with $Zn_{0.5}Ge_{0.5}P$. The XPS results indicate that Zn-P and Ge-P bonds of $Zn_{0.5}Ge_{0.5}P$ are broken after lithiation, and Li-Zn, Li-Ge, and Li-P bonds are seen due to the formation of the LiZn, $Li_{15}Ge_4$, and Li_3P species.

We further performed ex-situ HR-TEM and fast Fourier transform (FFT) to identify the intermediate phases. As shown in **Fig. 4a-l**, the potential-dependent HR-TEM images with FFT spot patterns were collected during the first discharging-charging cycle. When the cell was discharged to 0.4 V, there are two phases generated, Li_3P and LiZnGe. As shown in **Fig. 4a**, the lattice fringes show a characteristic spacing of 3.79 Å for (002) lattice planes of hexagonal-structured Li_3P and the FFT spot pattern of the selected area can be indexed to $[\bar{1}00]$ zone axis. In **Fig. 4b**, lattice fringes with the lattice spacing of 3.12 Å and 3.70 Å match well with (003) and (010) planes of hexagonal LiZnGe and the FFT spot pattern of the selected area can be indexed to the [100] zone axis.[44] Both of the Li_3P and LiZnGe are a layer-structured Li-ion compound which were considered as lithium-ion conductors that help to improve the reaction kinetics. After being discharged 0.35 V, β-Li_2ZnGe was observed, as shown in **Fig. 4c**. The lattice fringes with a lattice spacing of 5.49 Å match well with the (003) plane of hexagonal β-Li_2ZnGe and the FFT spot pattern of the selected area can be indexed to [100] zone axis.[42] When discharged to 0.3 V, the cubic α-Li_2ZnGe is generated, as shown in **Fig. 4d**. The lattice fringes with the lattice spacing of 3.12 Å match well with (111) and $(11\bar{1})$ planes at 71° of the cubic Li_2ZnGe phase, and the FFT spot pattern of the selected area can be indexed to $[1\bar{1}0]$ zone axis. When fully discharged to 0 V, as shown in **Fig. 4e**, **4f**, and **4g**, the discharging products are LiZn, $Li_{15}Ge_4$, and Li_3P, which are consistent with the XRD results. During charging, as shown in **Fig. 4h**, **4i**, **4j**, and **4k**, LiZn and $Li_{15}Ge_4$ phases disappear. LiZnGe, α-Li_2ZnGe, and β-Li_2ZnGe phases are reformed at 0.7 V. When

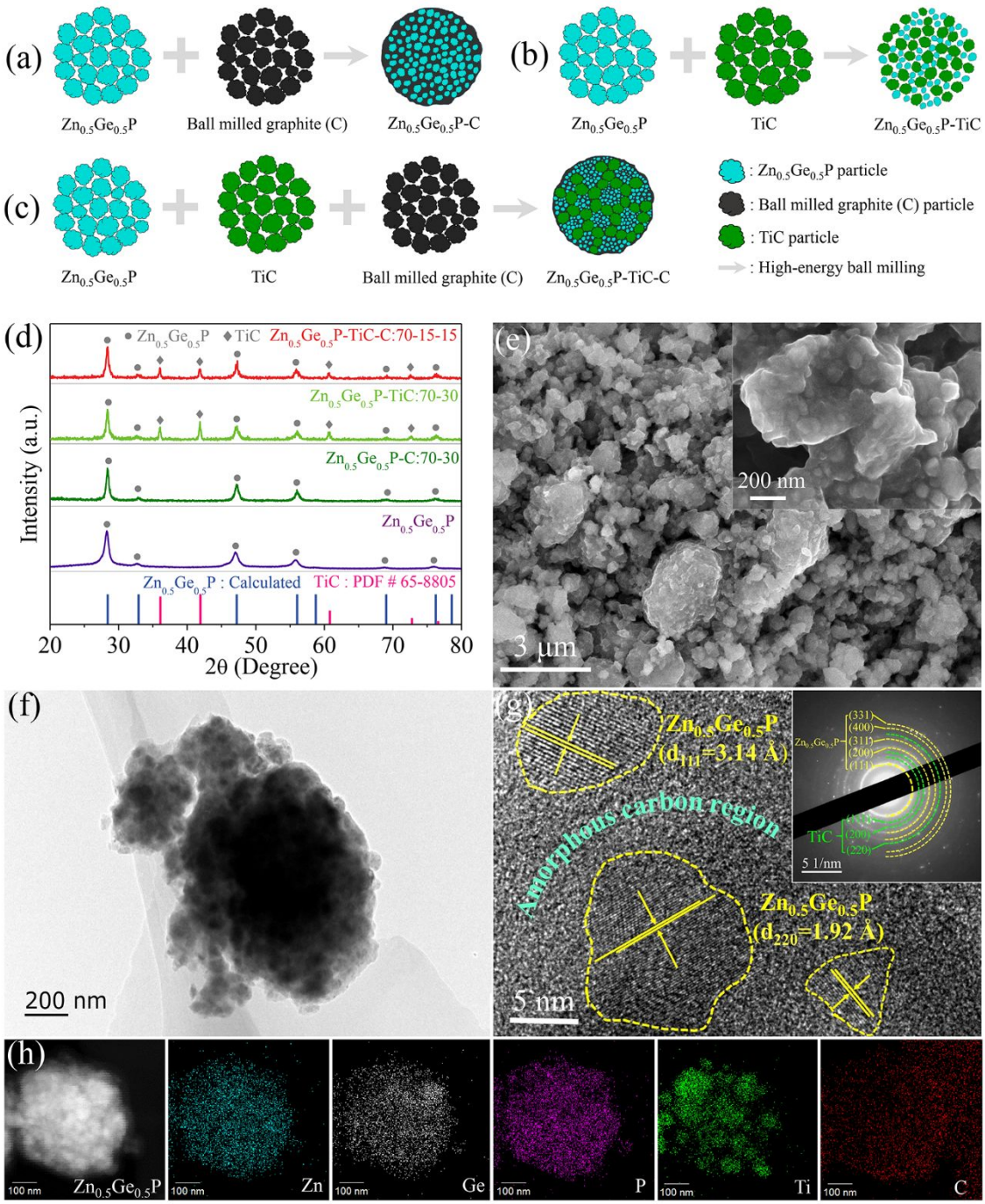

Fig. 5 Schematic diagram formation process of (a) $Zn_{0.5}Ge_{0.5}P$-C, (b) $Zn_{0.5}Ge_{0.5}P$-TiC, and (c) $Zn_{0.5}Ge_{0.5}P$-TiC-C; (d) The XRD results of the $Zn_{0.5}Ge_{0.5}P$, $Zn_{0.5}Ge_{0.5}P$-C, $Zn_{0.5}Ge_{0.5}P$-TiC, and $Zn_{0.5}Ge_{0.5}P$-TiC-C electrodes; (e) SEM images of the $Zn_{0.5}Ge_{0.5}P$-TiC-C; (f) and (g) TEM image of $Zn_{0.5}Ge_{0.5}P$-TiC-C nanocomposite; (h) The EDS mapping images of each element of Zn, Ge, P, Ti, and C.

fully charged back to 3 V, $Zn_{0.5}Ge_{0.5}P$ is reconstructed. For the phases of LiZnGe, α-Li_2ZnGe, and β-Li_2ZnGe, all of them show the metallic conductivity with a bandgap of 0 eV. LiZnGe and β-Li_2ZnGe with lithium-ion transport channel crystallized in layered hexagonal structure and the α-Li_2ZnGe crystallized in cubic structure. The electrochemical transformation between the α-Li_2ZnGe and β-Li_2ZnGe was reported previously.[42, 47, 48] These intermediates of Li_3P, LiZnGe, α-Li_2ZnGe, and β-Li_2ZnGe with lithium-ion transport channels will benefit the transfer of lithium-ion transfer and improve the lithiation/delithiation process.

From these experiments, a reaction mechanism is suggested in **Fig. 4m** and is given by the following equation:

$Zn_{0.5}Ge_{0.5}P + Li^+ + e^- \rightleftharpoons Li_xZn_{0.5}Ge_{0.5}P$, (Amorphization, $0 < x \leq 1$) (1)

$Li_xZn_{0.5}Ge_{0.5}P + Li^+ + e^- \rightleftharpoons$ LiZnGe + α-Li_2ZnGe + β-Li_2ZnGe + Li_3P, (Conversion) (2)

LiZnGe + α-Li_2ZnGe + β-Li_2ZnGe + $Li_3P + Li^+ + e^- \rightleftharpoons$ LiZn + $Li_{15}Ge_4$ + Li_3P, (Alloying) (3)

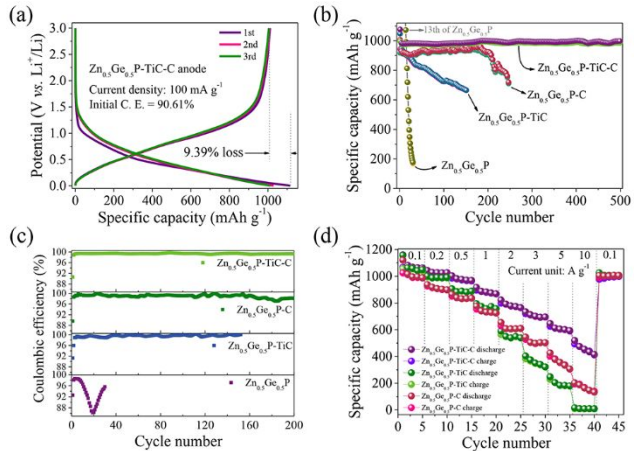

Fig. 6 (a) Galvanostatic discharge-charge profiles of $Zn_{0.5}Ge_{0.5}P$-TiC-C electrode *vs.* Li using 1 M $LiPF_6$ in EC/DEC as electrolyte; (b) Comparison of cycle performance with the corresponding Coulombic efficiency of (c); (d) The rate performance of $Zn_{0.5}Ge_{0.5}P$, $Zn_{0.5}Ge_{0.5}P$-C, $Zn_{0.5}Ge_{0.5}P$-TiC, and $Zn_{0.5}Ge_{0.5}P$-TiC-C electrodes.

To enhancing the electrochemical performances of $Zn_{0.5}Ge_{0.5}P$, TiC and amorphous carbon (C) were used to synthesize $Zn_{0.5}Ge_{0.5}P$-TiC-C nanocomposites. As illustrated in **Fig. 5a-c**, the introduced milled C acts as a matrix to disperse the agglomerated $Zn_{0.5}Ge_{0.5}P$ particles and reduce the particle size during the milling process (**Fig. 5a**). The introduced super-hard TiC can be a milling aid to reduce the particle size and improve the uniformity of the Zinc blended $Zn_{0.5}Ge_{0.5}P$ (**Fig. 5b**). These additives also prevent the agglomeration of $Zn_{0.5}Ge_{0.5}P$ particles (**Fig. 5c**).

The XRD patterns of the synthesized composite are shown in **Fig. 5d**. No noticeable graphite peaks are shown since carbon stays in the amorphous state. All patterns show $Zn_{0.5}Ge_{0.5}P$ peaks, which means that $Zn_{0.5}Ge_{0.5}P$ remains the crystalline state after milling with C and TiC. For the $Zn_{0.5}Ge_{0.5}P$-TiC and $Zn_{0.5}Ge_{0.5}P$-TiC-C composites, several peaks, corresponding to TiC (PDF #65-8805) at 35.9°, 41.7°, are detected in addition to $Zn_{0.5}Ge_{0.5}P$ peaks, which proves that the introduced TiC remains crystalline state after milling. SEM images of $Zn_{0.5}Ge_{0.5}P$-TiC-C (**Fig. 5e**) reveal that it consists of many primary particles with the size of 50 - 100 nm, and forms the secondary particles with sizes ranging from several hundred nanometers to microns. $Zn_{0.5}Ge_{0.5}P$-TiC-C shows smaller particle size than that of the synthesized $Zn_{0.5}Ge_{0.5}P$, $Zn_{0.5}Ge_{0.5}P$-C and $Zn_{0.5}Ge_{0.5}P$-TiC (show in **Fig. S7 a**, **b**, and **c**). TEM images (**Fig. 5f)** also show that the $Zn_{0.5}Ge_{0.5}P$-TiC-C nanocomposite particles consist of many aggregated primary small particles. The HRTEM image (**Fig. 5g**) clearly shows the lattice fringes of the $Zn_{0.5}Ge_{0.5}P$ phase with an interplanar spacing of 0.314 nm and 0.192 nm, which is well-matched to the (111) and (220) planes respectively, and a grain size of the $Zn_{0.5}Ge_{0.5}P$ is about 5-10 nm. The selected area electron diffraction (SAED) patterns of the Zinc blended $Zn_{0.5}Ge_{0.5}P$-TiC-C is shown in **Fig. 5g**. Polycrystalline $Zn_{0.5}Ge_{0.5}P$ and TiC are revealed by the diffraction rings. Also, energy-dispersive spectroscopy (EDS) mapping images **(Fig. 5h**) show that the Zinc blended $Zn_{0.5}Ge_{0.5}P$ nano-crystallites are uniformly dispersed within the amorphous carbon matrix with TiC as a backbone to maintain the structure.

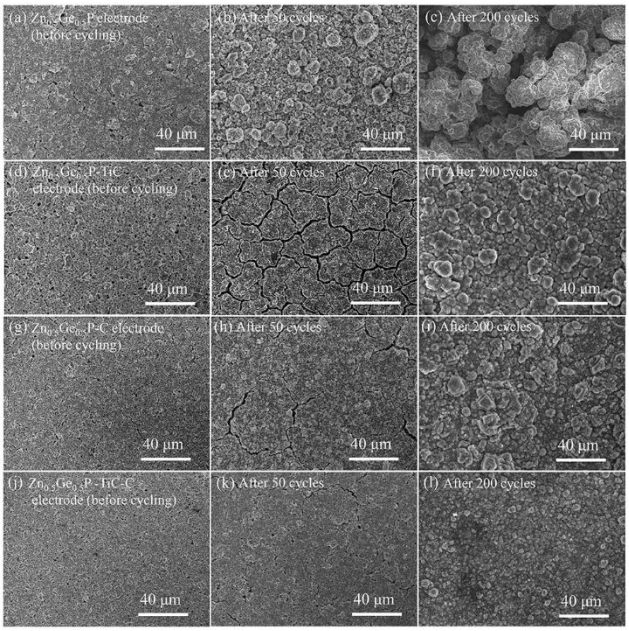

Fig. 7 Surface morphology change of $Zn_{0.5}Ge_{0.5}P$, $Zn_{0.5}Ge_{0.5}P$-C, $Zn_{0.5}Ge_{0.5}P$-TiC, and $Zn_{0.5}Ge_{0.5}P$-TiC-C electrodes after different cycle number (*vs.* Li using 1 M $LiPF_6$ in EC/DEC as electrolyte).

To evaluate the electrochemical performance of $Zn_{0.5}Ge_{0.5}P$, $Zn_{0.5}Ge_{0.5}P$-C, $Zn_{0.5}Ge_{0.5}P$-TiC, and $Zn_{0.5}Ge_{0.5}P$-TiC-C electrodes, galvanostatic charge and discharge experiments were performed within a voltage range of 0 - 3.0 V (vs. Li^+/Li). The voltage profiles of those four electrodes are shown in **Fig. 6a**, **Fig. S8a**, 8**b**, and 8**c**, respectively. The results show that the charge-discharge curves of $Zn_{0.5}Ge_{0.5}P$-based anodes become smooth after the modification with TiC or C. The cycling performance and Coulombic efficiency of these four electrodes are shown in **Fig. 6b** and **6c**, respectively. $Zn_{0.5}Ge_{0.5}P$-TiC-C shows the best cycling performance with a capacity retention of 92.6% (vs. first discharged 1076 mA h g^{-1}) after 500 cycles. $Zn_{0.5}Ge_{0.5}P$-C, $Zn_{0.5}Ge_{0.5}P$-TiC and $Zn_{0.5}Ge_{0.5}P$ show poor capacity retention of 71.8%, 63.4% and 11.6% after 247, 151, and 30 cycles, respectively.

To explaining and understanding the differences of the cycling performance, the electrode surface morphology changes as a function of cycle number are observed. As shown in **Fig. 7**, all four types of electrodes show a smooth surface before cycling. After 50 cycles, obvious cracks are shown in $Zn_{0.5}Ge_{0.5}P$-TiC and $Zn_{0.5}Ge_{0.5}P$-C Zinc blended $Zn_{0.5}Ge_{0.5}P$ particles start to agglomerate. $Zn_{0.5}Ge_{0.5}P$-TiC-C maintains the same morphology as before cycling. After 200 cycles, the $Zn_{0.5}Ge_{0.5}P$ anode shows a loose and porous structure which leads to severe side effects and poor electrical contact, resulting in poor cycling performance. With the addition of TiC and C, the morphology of the $Zn_{0.5}Ge_{0.5}P$-TiC-C electrode remains stable and dense during cycling, preventing material agglomeration and maintaining electrical contact, resulting in improved cycling performance. **Fig. 6d** shows the rate capacity of the $Zn_{0.5}Ge_{0.5}P$-C, $Zn_{0.5}Ge_{0.5}P$-TiC, and $Zn_{0.5}Ge_{0.5}P$-TiC-C electrodes. $Zn_{0.5}Ge_{0.5}P$-TiC-C shows the best performance with a specific capacity of 520 mA h g^{-1} maintained at a high current density of 10 A g^{-1}. The specific capacity can be recovered to 1025 mA h g^{-1} as the current density further decreases to 0.1 A g^{-1}.

The superior rate capability of $Zn_{0.5}Ge_{0.5}P$-TiC-C draws our attention to understand the kinetics origin. **Fig. S9a** displays the cyclic voltammetry (CV) of the $Zn_{0.5}Ge_{0.5}P$-TiC-C electrode from 0.1 to 1.2 mV s^{-1}, and the shape is well preserved with increasing scan rate. The degree of capacitive effect can be qualitatively analyzed according to the relationship between measured current (i) and scan rate (v) from the CV curves: $i = av^b$, where a and b both are constants. The value of b is between 0.5 and 1, which is determined from the slope of the log i versus log v plot (**Fig. S9b**). It is well known that for a diffusion-controlled process b approaches 0.5, while for a surface capacitance-dominated process b is close to 1. Hence the b value of the $Zn_{0.5}Ge_{0.5}P$-TiC-C electrode suggests favored capacitive kinetics of pseudocapacitive lithium-ion storage. As shown in Fig. S9c, With the increase of the scan rate, the diffusion contribution is depressed, while the capacitive contribution increases as expected.

Conclusions

In summary, we have synthesized $Zn_{0.5}Ge_{0.5}P$ using mechanochemical synthesis. First-principles calculations reveal that high-symmetry $Zn_{0.5}Ge_{0.5}P$ shows superior electron and lithium-ion transport characteristics compared to $ZnGeP_2$, a related chalcopyrite allotrope. Based on these theoretical results, experiments were carried on the $Zn_{0.5}Ge_{0.5}P$ anode material, which exhibited a specific capacity of 1438 mA h g^{-1} with an initial Coulombic efficiency of 92%. $Zn_{0.5}Ge_{0.5}P$ experiences an amorphization-conversion-alloying reaction mechanism with Li. Crystallized $Zn_{0.5}Ge_{0.5}P$ gradually converted to amorphous $LixZn_{0.5}Ge_{0.5}P$ at the beginning of lithiation, then to LiZnGe, β-Li_2ZnGe, and α-Li_2ZnGe phases sequentially, finally formed alloyed phases of LiZn, $Li_{15}Ge_4$, and Li_3P. TiC is introduced and is able to refine the grain size of $Zn_{0.5}Ge_{0.5}P$, while C is introduced as a matrix to disperse $Zn_{0.5}Ge_{0.5}P$ particles and buffer volume change during cycling. The $Zn_{0.5}Ge_{0.5}P$-TiC-C composite anode exhibited an initial specific capacity of 1076 mA h g^{-1} and a capacity retention of 92.6% after 500 cycles. This work advances the development of high-energy, high-rate, and stable anodes for lithium-ion batteries.

Author contributions

All authors discussed the results, contributed to the manuscript writing, and approved its final version. W. Li and Z. shi supervised the project. G. Liu performed most of the experiments and wrote the original manuscript. L. Zhang conducted the first principles calculations and revised the manuscript. Y. Zhou, and Luke Soule revised the manuscript. Y. Mu assisted in some parts of the experiments.

Conflicts of interest

There are no conflicts to declare.

Acknowledgements

We gratefully acknowledge the financial support from the National Natural Science Foundation, China (21673051 and 21701030), Natural Science Foundation Project of Zhaoqing University (2020012518), and the Department of Science and Technology of Guangdong Province, China (2019A050510043). The authors acknowledge the use of facilities in Guangdong University of Technology, GDUT Analysis and Test Center. This research used resources of the National Energy Research Scientific Computing Center, a DOE Office of Science User Facility supported by the Office of Science of the U.S. Department of Energy under Contract No. DE-AC02-05CH11231.

Notes and references

1. W. Martin, B. Brian and X. Kang, *Chem. Rev.*, 2018, **118**, 11433-11456.
2. W. Feixiang, M. Joachim and Y. Yan, *Chem. Soc. Rev.*, 2020, **49**, 1569-1614.
3. M. Kühne, F. Börrnert, S. Fecher, M. Ghorbani-Asl, J. Biskupek, D. Samuelis, A. V. Krasheninnikov, U. Kaiser and J. H. Smet, *Nature*, 2018, **564**, 234-239.
4. Y. Li, Y. Lu, P. Adelhelm, M.-M. Titirici and Y.-S. Hu, *Chem. Soc. Rev.*, 2019, **48**, 4655-4687.
5. L. Xia, Z. Liang, H. Xiaoqing, X. Ruijuan, G. Lin, H. Yong‐Sheng, L. Hong, W. Zhaoxiang, D. Xiaofeng, C. Liquan, M. Joachim and I. Yuichi, *Adv. Mater.*, 2012, **24**, 3233-3238.
6. T. Yuan, Z. Tan, C. Ma, J. Yang, Z.-F. Ma and S. Zheng, *Adv. Energy Mater.*, 2017, **7**, 1601625.
7. A. W. Xiao, H. J. Lee, I. Capone, A. Robertson, T. U. Wi, J. Fawdon, S. Wheeler, H. W. Lee, N. Grobert and M. Pasta, *Nat. Mater.*, 2020, **19**, 644-654.
8. J. Cabana, L. Monconduit, D. Larcher and M. R. Palacin, *Adv. Mater.*, 2010, **22**, E170-192.
9. C. M. Park, J. H. Kim, H. Kim and H. J. Sohn, *Chem. Soc. Rev.*, 2010, **39**, 3115-3141.
10. M. R. Palacin, *Chem. Soc. Rev.*, 2009, **38**, 2565-2575.
11. D. Bresser, S. Passerini and B. Scrosati, *Energy Environ. Sci.*, 2016, **9**, 3348-3367.
12. D. Rehnlund, F. Lindgren, S. Böhme, T. Nordh, Y. Zou, J. Pettersson, U. Bexell, M. Boman, K. Edström and L. Nyholm, *Energy Environ. Sci.*, 2017, **10**, 1350-1357.
13. Y. Hwa, J. H. Sung, B. Wang, C.-M. Park and H.-J. Sohn, *J. Mater. Chem.*, 2012, **22**, 12767.
14. S. O. Kim and A. Manthiram, *ACS Appl. Mater. Interfaces*, 2015, **7**, 14801-14807.
15. L. Y. Lim, S. Fan, H. H. Hng and M. F. Toney, *Adv. Energy Mater.*, 2015, **5**, 1500599.
16. M.-H. Seo, M. Park, K. T. Lee, K. Kim, J. Kim and J. Cho, *Energy Environ. Sci.*, 2011, **4**, 425-428.
17. W. Lei, G. Liu, J. Zhang and M. Liu, *Chem. Soc. Rev.*, 2017, **46**, 3492-3509.
18. G. L. Xu, Z. Chen, G. M. Zhong, Y. Liu, Y. Yang, T. Ma, Y. Ren, X. Zuo, X. H. Wu, X. Zhang and K. Amine, *Nano Lett.*, 2016, **16**, 3955-3965.
19. S. Zhang, Y. Zheng, X. Huang, J. Hong, B. Cao, J. Hao, Q. Fan, T. Zhou and Z. Guo, *Adv. Energy Mater.*, 2019, **9**, 1900081.
20. C. Peng, H. Chen, G. Zhong, W. Tang, Y. Xiang, X. Liu, J. Yang, C. Lu and Y. Yang, *Nano Energy*, 2019, **58**, 560-567.

21. W. Li, J. Yu, J. Wen, J. Liao, Z. Ye, B. Zhao, X. Li, H. Zhang, M. Liu and Z. Guo, *J. Mater. Chem.*, 2019, **7**, 16785-16792.
22. C. M. Park and H. J. Sohn, *Chem. Mater.*, 2008, **20**, 6319-6324.
23. W. Li, L. Gan, K. Guo, L. Ke, Y. Wei, H. Li, G. Shen and T. Zhai, *Nanoscale*, 2016, **8**, 8666-8672.
24. M. V. V. M. Satya Kishore and U. V. Varadaraju, *J. Power Sources*, 2005, **144**, 204-207.
25. W. Li, X. Li, J. Yu, J. Liao, B. Zhao, L. Huang, A. Ali, H. Zhang, J. H. Wang, Z. Guo and M. Liu, *Nano Energy*, 2019, **61**, 594-603.
26. H. Shen, Y. Huang, Y. Chang, R. Hao, Z. Ma, K. Wu, P. Du, B. Guo, Y. Lyu, P. Wang, H. Yang, Q. Li, H. Wang, Z. Liu and A. Nie, *ACS Appl. Mater. Interfaces*, 2020, **12**, 17466-17473.
27. X. Deng, X. Chen, Y. Huang, B. Xiao and H. Du, *The Journal of Physical Chemistry C*, 2019, **123**, 4721-4728.
28. K.-H. Nam, K.-J. Jeon and C.-M. Park, *Energy Storage Materials*, 2019, **17**, 78-87.
29. S. Haghighat-Shishavan, M. Nazarian-Samani, M. Nazarian-Samani, H. K. Roh, K. Y. Chung, S. H. Oh, B. W. Cho, S. F. Kashani-Bozorg and K. B. Kim, *ACS Appl. Mater. Interfaces*, 2019, **11**, 32815-32825.
30. W. Li, H. Li, Z. Lu, L. Gan, L. Ke, T. Zhai and H. Zhou, *Energy Environ. Sci.*, 2015, **8**, 3629-3636.
31. W. Li, X. Li, J. Liao, B. Zhao, L. Zhang, L. Huang, G. Liu, Z. Guo and M. Liu, *Energy Environ. Sci.*, 2019, **12**, 2286-2297.
32. W. Li, J. Liao, X. Li, L. Zhang, B. Zhao, Y. Chen, Y. Zhou, Z. Guo and M. Liu, *Adv. Funct. Mater.*, 2019, **29**, 1903638.
33. M. Zhang, R. Hu, J. Liu, L. Ouyang, J. Liu, L. Yang and M. Zhu, *Electrochem. Commun.*, 2017, **77**, 85-88.
34. A. D. Martinez, A. N. Fioretti, E. S. Toberer and A. C. Tamboli, *J. Mater. Chem.*, 2017, **5**, 11418-11435.
35. T. Basak, M. N. Rao and S. L. Chaplot, *J. Phys. Conf. Ser.*, 2012, **377**, 012071.
36. I. T. Kim, S.-O. Kim and A. Manthiram, *J. Power Sources*, 2014, **269**, 848-854.
37. S. Y. Son, J. Hur, K. H. Kim, H. B. Son, S. G. Lee and I. T. Kim, *J. Power Sources*, 2017, **365**, 372-379.
38. G. Kresse and F. J, *Physical Review B*, 1996, **54**, 11169-11186.
39. E. Buehler, J. H. Wernick and J. D. Wiley, *J. Electron. Mater.*, 1973, **2**, 445-454.
40. C. Suryanarayana, *Prog. Mater Sci.*, 2001, **46**, 1-184.
41. C. J. Wen, B. Boukamp, R. A. Huggins and W. Weppner, *J. Electrochem. Soc.*, 1979, **126**, 2258.
42. R. Alcántara, M. Tillard-Charbonnel, L. Spina, C. Belin and J. L. Tirado, *Electrochim. Acta*, 2002, **47**, 1115-1120.
43. S.-Z. Yang, W. Sun, Y.-Y. Zhang, Y. Gong, M. P. Oxley, A. R. Lupini, P. M. Ajayan, M. F. Chisholm, S. T. Pantelides and W. Zhou, *Phys. Rev. Lett.*, 2019, **122**.
44. L. Lacroix-Orio, M. Tillard and C. Belin, *Solid State Sci.*, 2006, **8**, 208-215.
45. S. Shirakata, *J. Appl. Phys.*, 1999, **85**, 3294-3300.
46. W. K. Kuhn, *Surf. Sci. Spectra*, 1994, **3**, 93-99.
47. L. Lacroix-Orio, M. Tillard and C. Belin, *J. Alloys Compd.*, 2008, **465**, 47-50.
48. F. Kalarasse, L. Kalarasse, B. Bennecer and A. Mellouki, *Comput. Mater. Sci*, 2010, **47**, 869-874.